
CONFORMAL PREDICTION FOR ENSEMBLES: IMPROVING EFFICIENCY VIA SCORE-BASED AGGREGATION

Eduardo Ochoa Rivera*

Department of Statistics
University of Michigan
Ann Arbor, MI 48104
ochoa@umich.edu

Yash Patel**

Department of Statistics
University of Michigan
Ann Arbor, MI 48104
yppatel@umich.edu

Ambuj Tewari

Department of Statistics
University of Michigan
Ann Arbor, MI 48104
tewaria@umich.edu

ABSTRACT

Distribution-free uncertainty estimation for ensemble methods is increasingly desirable due to the widening deployment of multi-modal black-box predictive models. Conformal prediction is one approach that avoids such distributional assumptions. Methods for conformal aggregation have in turn been proposed for ensembled prediction, where the prediction regions of individual models are merged as to retain coverage guarantees while minimizing conservatism. Merging the prediction regions directly, however, sacrifices structures present in the conformal scores that can further reduce conservatism. We, therefore, propose a novel framework that extends the standard scalar formulation of a score function to a multivariate score that produces more efficient prediction regions. We then demonstrate that such a framework can be efficiently leveraged in both classification and predict-then-optimize regression settings downstream and empirically show the advantage over alternate conformal aggregation methods.

1 Introduction

Ensemble methods are an oft-used class of statistical modeling techniques due to their ability to reduce variance or improve predictive accuracy [1, 2, 3]. Such methods are increasingly being coupled with complex, black-box models, such as in multi-modal language models [4, 5, 6, 7, 8]. Couplings of this sort are seeing ever-widening deployment in safety-critical settings, such as medicine [9, 10, 11] and robotics [12, 13, 14].

Increasing interest is, therefore, now being placed on quantifying uncertainty for such models [15, 16, 17, 18, 19]. Towards this end, methods of uncertainty quantification have arisen, such as deep ensembles and committee estimation [20, 21, 22]. Such methods, however, sacrifice generality with the imposition of distributional assumptions, motivating the need for distribution-free uncertainty quantification for ensemble methods.

One method for performing distribution-free uncertainty quantification is conformal prediction, which provides a principled framework for producing distribution-free prediction regions with marginal frequentist coverage guarantees [23, 24]. By using conformal prediction on a user-defined score function, prediction regions attain marginal coverage guarantees. While calibration is guaranteed from this procedure, predictive efficiency, quantified as the size of the resulting prediction regions, can be unboundedly large for poorly chosen score functions.

As a result, methods have arisen to perform conformal model aggregation, which both provide uncertainty estimates of the ensembled predictions and do so in ways as to minimize the prediction region size [25, 26, 27, 28, 29]. While such approaches succeed in reducing the prediction region size over naive aggregation, they all aggregate the *separately conformalized* prediction regions of the predictors in the ensemble. In doing so, they forgo the possibility of automatically leveraging shared structure amongst the scores of the individual predictors, resulting in overly conservative prediction regions.

We instead propose to perform aggregation in *score space* by extending traditional conformal prediction to consider a multivariate score function and defining prediction regions using “quantile envelopes” in place of scalar quantiles.

*Denotes alphabetic ordering indicating equal contributions.

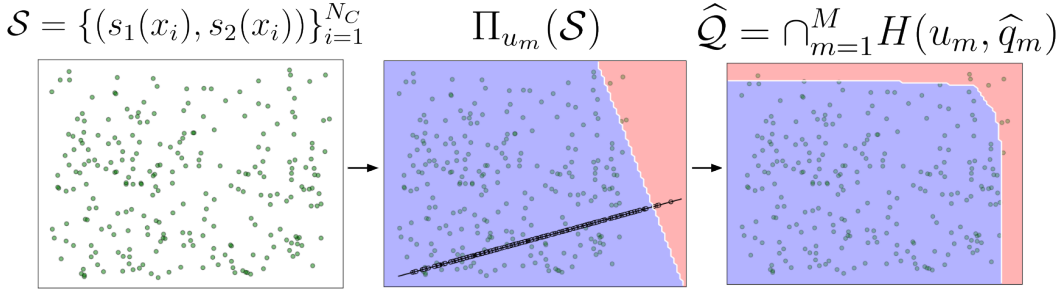


Figure 1: CSA provides a principled extension to the standard conformal prediction pipeline by leveraging ideas from higher-dimensional quantile regression to define quantile envelopes \hat{Q} instead of scalar quantiles \hat{q} . It does so by evaluating a collection of score functions (here s_1 and s_2) over the calibration dataset to define \mathcal{S} , finding quantiles $\{\hat{q}_m\}$ over a set of projection directions $\{u_m\}$, and taking \hat{Q} to be the intersection of the resulting half-planes $H(u_m, \hat{q}_m)$. These quantile envelopes result in more informative prediction regions that can be used in downstream tasks.

Doing so enables efficient, data-driven, automated conformal model aggregation. We demonstrate that this formulation retains the desired distribution-free coverage guarantees typical of standard conformal prediction and that the resulting prediction regions can be used efficiently in both classification and regression settings. Our contributions, thus, are:

- Providing a multivariate extension to conformal prediction, dubbed “conformal score aggregation” (CSA), that leverages quantile envelopes to enable data-driven, informative uncertainty estimation for model ensembles while retaining coverage guarantees.
- Demonstrating how the prediction regions resulting from CSA can be efficiently leveraged in downstream predict-then-optimize regression tasks.
- Demonstrating the empirical improvement of the CSA framework over alternate conformal aggregation strategies across classification and regression settings.

2 Background

2.1 Conformal Prediction

Coverage guarantees of uncertainty quantification methods generally rely on distributional assumptions, often via asymptotics or explicit specification. To alleviate the need for such restrictive assumptions, interest in finite-sample, distribution-free uncertainty quantification methods has risen. Conformal prediction is one such method [23, 24]. Due to its lack of structural assumptions, conformal prediction pairs well with the increasingly common black-box style of modeling.

Conformal prediction serves as a wrapper around such predictors, producing prediction regions $\mathcal{C}(x)$ that have formal guarantees of the form $\mathcal{P}_{X,Y}(Y \notin \mathcal{C}(X)) \leq \alpha$ for some prespecified level α . To achieve this, “split conformal” partitions the dataset $\mathcal{D} = \{(x_i, y_i)\}_{i=1}^N$ into a training set \mathcal{D}_T and a calibration set \mathcal{D}_C . The former serves as the data used to fit \hat{f} . Users of conformal prediction must then design a “score function” $s(x, y)$, which should quantify “test error”, often in a domain-specific manner. For instance, a simple score function for a regression setting would be $s(x, y) = \|\hat{f}(x) - y\|$. This score function is then evaluated across the calibration set to define $\mathcal{S}_C = \{s(x, y) \mid (x, y) \in \mathcal{D}_C\}$. For a desired coverage of $1 - \alpha$, we then take \hat{q} to be the $\lceil (|\mathcal{D}_C| + 1)(1 - \alpha) \rceil / |\mathcal{D}_C|$ quantile of \mathcal{S}_C , with which prediction regions for future test queries x can be defined as $\mathcal{C}(x) = \{y \mid s(x, y) \leq \hat{q}\}$. Under the exchangeability of the score of a test point $s(X', Y')$ with \mathcal{S}_C , we have the desired *finite-sample* probabilistic guarantee that $1 - \alpha \leq \mathcal{P}_{X', Y'}(Y' \in \mathcal{C}(X'))$.

While this guarantee holds for any $s(x, y)$, the informativeness of the resulting prediction regions, quantified as the inverse expected Lebesgue measure across X , i.e. $(\mathbb{E}[\mathcal{L}(\mathcal{C}(X))])^{-1}$, is intimately tied to its specification [24]. Thus, much of the challenge of conformal prediction relates to choosing a score function that retains coverage while minimizing region size.

2.2 Quantile Envelopes

Generalizations of quantiles have a long history in statistics [30, 31]. Unlike univariate data, multivariate data does not lend itself to an unambiguous definition of a quantile, as there is no canonical ordering in higher dimensional spaces. To account for this, one class of multivariate quantiles, known as “direction quantiles,” prescribes directions along which data points can be compared [32, 33, 34]. That is, points $x \in \mathbb{R}^n$ are projected along some direction $u \in \mathcal{S}^{n-1}$, after which the standard notion of a quantile can be leveraged.

The notion of the α quantile for a random variable $X \in \mathcal{X}$ clearly then depends on this choice of direction u , which we denote by $Q(X, \alpha, u) = \inf\{q \in \mathbb{R} : \mathcal{P}(u^\top X \leq q) \geq \alpha\}$. When there is no ambiguity, we just denote it as $Q(\alpha, u)$. In cases where domain knowledge assigns an unambiguous notion of multivariate ordering, such knowledge can be encoded into the choice of u . In other cases, however, a more agnostic approach is employed: rather than choosing any particular direction, all directions are considered simultaneously. For any given u , notice the choice of quantile defines a corresponding halfplane $H(u, Q(\alpha, u)) = \{x \in \mathcal{X} : u^\top x \leq Q(\alpha, u)\}$. To consider all directions simultaneously, the quantile envelope is then defined to be

$$D(\alpha) = \bigcap_{u \in \mathcal{S}^{n-1}} H(u, Q(\alpha, u)). \quad (1)$$

Notably, while each individual $H(u, Q(\alpha, u))$ captures $1 - \alpha$ of the points, $D(\alpha)$ does *not*, as it is the intersection thereof and hence captures $< 1 - \alpha$ of the mass. If $1 - \alpha$ combined coverage is sought, a correction, such as Bonferroni adjustment, is used for the individual planes.

2.3 Predict-Then-Optimize

Prediction regions produced from conformalized predictors are often leveraged differently across classification and regression settings. In the case of classification, “regions” simply constitute a subset of the label space, making their direct use by end users straightforward, as demonstrated in works such as [35]. In high-dimensional regression settings, however, prediction regions become harder to use directly; for this reason, recent works have started shifting focus to using them in their implicit forms.

One such application is [36], where conformal prediction was leveraged in a predict-then-optimize setting. As the name suggests, predict-then-optimize problems are two-stage problems, which take observed contextual information x and predict the parametric specification of a downstream problem of interest $\hat{c} := g(x)$ with some trained predictor g . The final result is then a decision made with this specification, $w^* := \min_w f(w, \hat{c})$. An example of such a setting is if an optimal labor allocation w^* is sought based on predicted demand \hat{c} from observed transactions x in a food delivery platform.

While the predicted \hat{c} is often simply trusted in the downstream optimization, this approach is inappropriate in risk-sensitive settings, where misspecification of the map $g : \mathcal{X} \rightarrow \mathcal{C}$ could lead to suboptimal decision-making. For this reason, recent interest has been placed on studying a “robust” alternative to this formulation [37, 38, 39]. Following this line of work, [36] proposed studying $w^*(x) := \min_w \max_{\hat{c} \in \mathcal{C}(x)} f(w, \hat{c})$, with $\mathcal{C}(x)$ being produced by conformalizing the predictor g . The primary consequence of doing so was having a probabilistic guarantee on the suboptimality gap. That is, denoting the suboptimality gap by $\Delta(x, c) := \min_w \max_{\hat{c} \in \mathcal{C}(x)} f(w, \hat{c}) - \min_w f(w, c)$, where c is the true parameter corresponding to x , they established that leveraging conformal uncertainty regions guarantees $\mathcal{P}_{X, C} (0 \leq \Delta(X, C) \leq L \text{ diam}(\mathcal{C}(X))) \geq 1 - \alpha$ if $f(w, c)$ is an objective function that is convex-concave and L -Lipschitz in c for any fixed w .

2.4 Related Works

Ensemble methods consist of K predictors $f_k : \mathcal{X}_k \rightarrow \mathcal{Y}$; notably, such predictors need not map from the same set of covariates. A naive approach for uncertainty quantification would then be to conformalize the ensembled predictor. That is, for an ensembling algorithm $\mathcal{F} : \mathcal{Y}^K \rightarrow \mathcal{Y}$, a score function $s(\mathcal{F}(f_1(x), \dots, f_K(x)), y)$ would be defined. Denoting the $\lceil (N_C + 1)(1 - \alpha) \rceil / N_C$ quantile of the score distribution over \mathcal{D}_C as $\hat{q}(\alpha)$, $\mathcal{C}(x) = \{y : s(x, y) \leq \hat{q}(\alpha)\}$ would then be marginally calibrated.

Such an approach, however, lacks some desirable properties. In particular, prediction regions $\mathcal{C}(x)$ should have the quality that, if a particular predictor has less uncertainty in its predictions, as is frequently true of ensemble settings where the predictors span multiple input data modalities, upon routing to that predictor, the corresponding size of the prediction region should be smaller than if it had been routed to a different predictor. While the naive approach does, in principle, support this property, it ultimately relies on defining an *uncertainty-aware* ensembling algorithm \mathcal{F} .

In its typical form, however, \mathcal{F} simply takes *point predictions* $f_1(x), \dots, f_K(x)$ in as input, meaning any uncertainty-awareness would need to be baked in a priori into the definition of \mathcal{F} through domain knowledge of the uncertainties of the predictors f_1, \dots, f_K , which can seldom be specified precisely, sacrificing the predictive efficiency of $\mathcal{C}(x)$.

Conformal model aggregation, thus, seeks to mitigate these deficiencies by aggregating the prediction regions $\mathcal{C}_1(x), \dots, \mathcal{C}_K(x)$ rather than the individual point predictions [25, 27, 28, 29]. While there are several methods in this vein, they can be categorized into one of two general approaches. The first line of work seeks to perform model *selection*, in which a single conformal predictor is selected \mathcal{C}_{k^*} , typically based on the criterion of minimizing region size $k^* := \arg \min_k \mathbb{E}[\mathcal{L}(\mathcal{C}_k(X))]$ [27, 28]. Generally, however, methods leveraging the full collection of predictors produce less conservative regions [25, 29]. Such works aggregate the individual prediction regions into a final region by defining

$$\mathcal{C}(x) := \left\{ y \mid \sum_{k=1}^K w_k \mathbb{1}[y \in \mathcal{C}_k(x)] \geq \hat{a} \right\} \quad (2)$$

for weights $\{w_k\} \in [0, 1]$ such that $\sum_{k=1}^K w_k = 1$ and a threshold \hat{a} . Methods then differ in the procedure by which $\{w_k\}$ and \hat{a} are prescribed, several of which were prescribed in [29], whose detailed presentation is deferred to Appendix F for space reasons. We note that the methods of [25] are designed for a different setting than that considered herein, namely that in which conformal coverage is sought adaptively over online data streams.

In this vein, [40] is a recent work that has similarly proposed a vector-score extension as that discussed herein, in which candidate weight vectors $\{w_m\} \in \mathbb{R}^K$ are searched over for score aggregation. That is, a vector $s(x) := (s_1(x, y), \dots, s_K(x, y)) \in \mathbb{R}^K$ of scores $s_k(x, y)$ corresponding to each predictor $f_k(x)$ is predicted and its aggregate prediction region defined on the projection $\langle w_{m^*}, s \rangle$ for w_{m^*} the weight resulting in the smallest prediction region. This method, however, has two shortcomings addressed herein. The first is that their method can only be applied in classification settings, whereas our method can be leveraged across both regression and classification problems. The second is that their approach only uses a *single* weighted projection in the end, resulting in suboptimal aggregation and, therefore, conservative prediction regions.

3 Method

We now introduce a procedure for conformal score aggregation for ensembles. We discuss the approach and its coverage guarantees in Section 3.1. We then discuss the downstream use of its prediction regions in Section 3.2.

3.1 Multivariate Score Quantile

We wish to consider the setting typical of conformal model aggregation, as discussed in Section 2.4, in which predictors $f_1(x), \dots, f_K(x)$ and corresponding scores $s_1(x, y), \dots, s_K(x, y)$ are defined. We further assume a similar premise as that taken by [40], in which the individual scores are stacked into a multivariate score $s(x, y) := (s_1(x, y), \dots, s_K(x, y))$. A naive approach would then involve leveraging standard conformal prediction over a pre-defined map $g : \mathbb{R}^K \rightarrow \mathbb{R}$, e.g., $g(s) = \sum_{k=1}^K s_k$. Similar to the naive conformalization of an ensembled predictor discussed in Section 2.4, using a *fixed* g fails to adapt to any disparities in uncertainties present across predictors or requires intimate knowledge of such uncertainties. We instead wish to provide a data-adaptive pipeline to automatically produce such a g .

Importantly, we heretofore assume the score functions are non-negative, i.e., $s_k : \mathcal{X} \times \mathcal{Y} \rightarrow \mathbb{R}_+$, which is typically the case as the score serves as a generalization of the residual. We highlight that many of the details of the method presented below are geometric in nature and are more easily understood with the supplement of diagrams. We have, thus, provided an accompanying visual walkthrough of the procedure in Appendix A to clarify its presentation.

3.1.1 Score Partial Ordering

Intuitively, our method seeks to directly generalize the approach of split conformal, by “ordering” the collection of multivariate calibration scores and taking the $1 - \alpha$ score under such an ordering to be a threshold \hat{Q} with which prediction regions are then implicitly defined. Formally, the multivariate “ordering” is established as a pre-ordering \lesssim over \mathbb{R}^K ; a pre-ordering differs from a total ordering in that it need not satisfy the antisymmetric axiom of a total ordering. Roughly speaking, an “acceptance region,” so called as it serves as the criterion used to ultimately decide which y are accepted into the prediction region, is then defined as $\hat{Q} := \{s \mid s \lesssim \hat{q}\}$, where \hat{q} is the $1 - \alpha$ empirical quantile of \mathcal{S}_C under \lesssim . Such a \hat{Q} naturally generalizes the standard scalar acceptance interval of $[0, \hat{q}]$ in the case of non-negative score functions. We briefly highlight the distinction between *acceptance regions* and *prediction regions*: the former are subsets of the space of multivariate scores, i.e. $\subset \mathbb{R}^K$, that ultimately define the criteria for retaining

particular y values in the prediction region whereas the latter are the subsets of the output space that ultimately have coverage guarantees, i.e. $\subset \mathcal{Y}$. The two, however, are directly related; in particular, for a fixed score $s(x, y)$, a larger acceptance region will result in a more conservative prediction region.

Crucially, therefore, the problem of choosing this pre-ordering closely parallels that of choosing g , where a poorly chosen pre-ordering will result in overly large acceptance regions and, hence, conservative prediction regions. For instance, using a lexicographical ordering \lesssim_{Lex} will result in axis-aligned hyper-rectangular acceptance regions. As a result, rather than manually prescribing a pre-ordering, we define \lesssim in a data-driven fashion by prescribing an indexed family of nested sets $\{\mathcal{A}_t\}_{t \in \mathbb{R}}$, such that $\mathcal{A}_{t_1} \subset \mathcal{A}_{t_2}$ for $t_1 \leq t_2$ and stating $s_1 \lesssim s_2$ if $\forall t, s_2 \in \mathcal{A}_t \implies s_1 \in \mathcal{A}_t$.

For a family of sets $\{\mathcal{A}_t\}_{t \in \mathbb{R}}$, we take each \mathcal{A}_t to be the region of the positive orthant \mathbb{R}_+^K bounded by the coordinate axes and an ‘‘outer frontier’’ parameterized by t . The shape of this outer frontier remains fixed over the family and is merely scaled outward from the origin with t . Under this choice, performing a comparison of $s_1, s_2 \in \mathbb{R}^K$ in the aforementioned fashion, i.e. checking if $s_1 \lesssim s_2$, amounts to checking if $t(s_1) \leq t(s_2)$, where $t(s)$ is the smallest t for which the outer frontier of \mathcal{A}_t intersects s . Notably, $t(s)$ is precisely the aforementioned data-driven score fusion function $g(s)$ of interest. Defining a data-adaptive $g(s)$, therefore, reduces to having a data-driven approach for defining the outer frontier of \mathcal{A}_t . We restrict this outer frontier to be such that \mathcal{A}_t is a convex set; if \mathcal{A}_t were permitted to be nonconvex, computing $t(s) := \min\{t \in \mathbb{R} : s \in \mathcal{A}_t\}$ would potentially be computationally expensive. The benefits of such convexity are highlighted, for example, in Section 3.2.

To have tight acceptance regions, we formally wish for the pre-ordering to have the property that the acceptance region given by $\tilde{\mathcal{Q}}$ has minimal Lebesgue measure and captures $1 - \alpha$ points of \mathcal{S}_C . The problem of discovering an optimal pre-ordering can, thus, be equivalently stated as seeking to define the outer frontier of \mathcal{A}_t to match that of the tightest $1 - \alpha$ convex cover of \mathcal{S}_C .

This final reframing, therefore, naturally motivates selecting the outer frontier to be the $1 - \alpha$ quantile envelope of \mathcal{S}_C . Using \mathcal{S}_C to define \mathcal{A}_t and in turn \lesssim , however, sacrifices the exchangeability of its points with future test scores s' , as the very nature of ordering would change in swapping s' with any $s \in \mathcal{S}_C$. The goal, then, follows as seeking to define the outer frontier as the $1 - \alpha$ quantile envelope of \mathcal{S}_C without directly using \mathcal{S}_C . For this reason, we partition $\mathcal{S}_C = \mathcal{S}_C^{(1)} \cup \mathcal{S}_C^{(2)}$, where we define \lesssim using $\mathcal{S}_C^{(1)}$ and compute the final \tilde{q} over $\mathcal{S}_C^{(2)}$. Such a split is predicated on the assumption that the $1 - \alpha$ quantile envelope defined over $\mathcal{S}_C^{(1)}$ resembles that of $\mathcal{S}_C^{(2)}$, implying the $|\mathcal{S}_C^{(1)}|$ should be sufficiently large as to capture this structure accurately.

We now focus attention on defining the quantile envelope over $\mathcal{S}_C^{(1)}$ using a technique paralleling that described in Section 2.2. In particular, we start by selecting the projection directions $\{u_m\}$ of Equation (1). The restriction of s to the positive orthant induces a natural modification of Equation (1), namely where $u \in \mathcal{S}_+^{K-1} := \mathcal{S}^{K-1} \cap \mathbb{R}_+^K$ instead of \mathcal{S}^{K-1} . To best approximate Equation (1), we wish for $\{u_m\}$ to be uniformly distributed over \mathcal{S}_+^{K-1} ; however, exactly finding an evenly distributed set of points over hyperspheres in arbitrary n -dimensional spaces is a classically difficult problem [41]. If $K = 2$, we can solve this exactly; for $K > 2$, we generate directions stochastically such that $U \sim \text{Unif}(\mathcal{S}_+^{K-1})$ by drawing $V_1, \dots, V_M \sim \mathcal{N}(0, I^{K \times K})$ and defining $U_i := V_i^{\|\cdot\|} / \sqrt{V_1^2 + \dots + V_M^2}$, where $v^{\|\cdot\|}$ denotes the component-wise absolute values of v .

We now wish to define the quantile thresholds $\{\tilde{q}_m\}$ for the selected directions to optimally capture $1 - \alpha$ of $\mathcal{S}_C^{(1)}$. Naively taking the $1 - \alpha$ quantile per projection direction u_m results in *joint* coverage by $\tilde{\mathcal{Q}} := \bigcap_{m=1}^M H(u_m, \tilde{q}_m)$ of $\mathcal{S}_C^{(1)}$ to be $< 1 - \alpha$. A straightforward fix is to replace the $1 - \alpha$ quantile per direction instead with its Bonferroni-corrected $1 - \alpha/M$ quantile. While valid, this approach produces overly conservative prediction regions. We, therefore, instead tune a separate $\beta \in (\alpha/M, \alpha)$ parameter via binary search, finding the maximum β^* such that using the β^* quantile per direction provides the overall desired coverage, i.e. $|\bigcap_{m=1}^M H(u_m, \tilde{q}_m(1 - \beta^*)) \cap \mathcal{S}_C^{(1)}| / N_{C_1} \in (1 - \alpha, 1 - \alpha + \epsilon)$ for some fixed, small $\epsilon > 0$. With this choice of $\{(u_m, \tilde{q}_m)\}$, we have a defined pre-ordering, whose coverage guarantees are formally stated below and proven in Appendix B.

Theorem 3.1. Suppose $\mathcal{D}_C := \{(X_i, Y_i)\}_{i=1}^{N_C}$ and (X', Y') are exchangeable. Assume further that K maps $s_k : \mathcal{X} \times \mathcal{Y} \rightarrow \mathbb{R}$ have been defined and a composite $s(X, Y) := (s_1(X, Y), \dots, s_K(X, Y))$ is defined. Further denote by \mathcal{S}_C the evaluation of $s(X, Y)$ on \mathcal{D}_C , namely $\mathcal{S}_C := \{s(X_i, Y_i) \mid (X_i, Y_i) \in \mathcal{D}_C\}$. For some $\alpha \in (0, 1)$, given a pre-order \lesssim in \mathbb{R}^K induced by a collection of nested sets $\{\mathcal{A}_t\}_{t \geq 0}$ define $\mathcal{Q}(\alpha) = \{s \in \mathbb{R}^K : s \lesssim s_{\lceil (N_C+1)(1-\alpha) \rceil}\}$. Then, denoting $\mathcal{C}(x) := \{y : s(x, y) \in \mathcal{Q}(\alpha)\}$, $\mathcal{P}_{X', Y'}(Y' \in \mathcal{C}(X')) \geq 1 - \alpha$.

3.1.2 Score Quantile Threshold

To then compute \hat{q} , we find $t^*(s)$ for each $s \in \mathcal{S}_C^{(2)}$, defined to be $\min\{t \in \mathbb{R} : s \in \bigcap_{m=1}^M H(u_m, t\tilde{q}_m)\}$. This can be efficiently computed as $t^*(s) = \max_{m=1, \dots, M} (u_m^\top s / \tilde{q}_m)$. Denoting the $\lceil (N_{C_2} + 1)(1 - \alpha) \rceil$ -th largest $t^*(s)$ as $\hat{t}, \hat{q}_m := \hat{t}\tilde{q}_m$ and $\hat{\mathcal{Q}} := \bigcap_{m=1}^M H(u_m, \hat{q}_m)$. If the tightest quantile envelope was already discovered over $\mathcal{S}_C^{(1)}$, this adjustment factor $\hat{t} \approx 1$.

Importantly, while the aforementioned procedure will necessarily result in convex regions $\hat{\mathcal{Q}}$, this does **not** mean the downstream prediction regions in \mathcal{Y} will be convex, as discussed in Section 3.2. Such flexibility is necessary, as many studies have demonstrated the need for nonconvex prediction regions for downstream utility, such as [36, 42, 43]. However, it is unsurprising such flexibility exists, as even a single *scalar* score $s_1(x, y)$ can produce nonconvex prediction regions. We present the full algorithm in Algorithm 1.

Algorithm 1 CSA: UNIFHYPERSPHERE(K) is an assumed subroutine that samples $\sim \text{Unif}(\mathcal{S}^{K-1})$.

```

1: Inputs: Score functions  $s_1, \dots, s_K : \mathcal{X} \rightarrow \mathcal{Y}$ , Calibration set  $\mathcal{D}_C$ , Desired coverage  $1 - \alpha$ 
2:  $[\beta_{\text{lo}}, \beta_{\text{hi}}] \leftarrow [\alpha/M, \alpha], \hat{\mathcal{Q}} \leftarrow \emptyset$ 
3:  $\mathcal{S}_C^{(1)} \cup \mathcal{S}_C^{(2)} \leftarrow \{(s_k(x_i, y_i))_{k=1}^K\}_{i=1, N_{C_1}+1}^{N_{C_1}, N_{C_2}}$ 
4:  $\{u_m \leftarrow \text{UNIFHYPERSPHERE}(K)\}_{m=1}^M$ 
5: while  $|\mathcal{S}_C^{(1)} \cap \hat{\mathcal{Q}}|/N_{C_1} \notin 1 - \alpha \pm \epsilon$  do
6:    $\beta \leftarrow \frac{\beta_{\text{lo}} + \beta_{\text{hi}}}{2}$ 
7:    $\left\{ \tilde{q}_m \leftarrow (1 - \beta) \text{ emp. quantile: } \{u_m^\top s_i\}_{s_i \in \mathcal{S}_C^{(1)}} \right\}_{m=1}^M$ 
8:    $\hat{\mathcal{Q}} \leftarrow \bigcap_{m=1}^M H(u_m, \tilde{q}_m)$ 
9:   if  $|\mathcal{S}_C^{(1)} \cap \hat{\mathcal{Q}}|/N_{C_1} > 1 - \alpha$  then  $\beta_{\text{lo}} \leftarrow \beta$ 
10:  else  $\beta_{\text{hi}} \leftarrow \beta$ 
11: end while
12:  $\hat{t} \leftarrow (1 - \alpha) \text{ emp. quantile: } \{\max_{m \in [M]} \frac{u_m^\top s_i}{\tilde{q}_m}\}_{s_i \in \mathcal{S}_C^{(2)}}$ 
13: Return  $\{(u_m, \hat{t}\tilde{q}_m)\}_{m=1}^M$ 

```

3.2 Predict-Then-Optimize

With this generalization of the score function, a natural question is how to leverage the resulting prediction regions $\mathcal{C}(x)$. For both classification and regression, $\mathcal{C}(x) = \{y \mid s(x, y) \in \hat{\mathcal{Q}}\}$, or $\mathcal{C}(x) = \bigcap_{m=1}^M \mathcal{C}_m(x)$ where $\mathcal{C}_m(x) := \{y \mid u_m^\top s(x, y) \leq \hat{q}_m\}$.

In the *classification* setting, where $|\mathcal{Y}| \in \mathbb{N}$, explicit construction of $\mathcal{C}(x)$ is straightforward. For a fixed x , explicitly constructing $\mathcal{C}(x)$ can be done by iterating through $y \in \mathcal{Y}$ and checking if $s(x, y) \in \hat{\mathcal{Q}}$ by comparing $s(x, y)$ against each one of the thresholds \hat{q}_m after projection.

In the case of regression, however, the prediction region cannot be explicitly constructed in the general case, since \mathcal{Y} contains uncountably many elements. In fact, explicit construction is generally not of interest for downstream regression applications. Instead, prediction regions in regression settings are often simply used in their implicit form. We, therefore, focus on one particular application, namely that of [36] discussed in Section 2.3, and demonstrate the CSA prediction regions can be leveraged in their framework. Such an extension has natural applications to the settings discussed in this original study. For instance, the authors demonstrated the utility of their method in a robust traffic routing setting with c being predicted traffic from a probabilistic weather model $q(C \mid X)$ for weather covariates X . An ensembling approach naturally emerges with having multiple predictive models, such as a $q_2(C \mid X)$ predicting traffic based instead on historical trends.

As in Section 3.1, we note that the below described algorithm is better understood with a visual accompaniment, which we provide in Appendix C. [36] demonstrated that solving the robust problem variant $w^*(x) := \min_w \max_{\hat{c} \in \mathcal{C}(x)} f(w, \hat{c})$ in a computationally efficient manner is feasible by performing gradient-based optimization on w , where the gradient $\nabla_w \phi(w)$ of $\phi(w) := \max_{\hat{c} \in \mathcal{C}(x)} f(w, \hat{c})$ can be computed by leveraging Danskin's Theorem so long as $\max_{\hat{c} \in \mathcal{C}(x)} f(w, \hat{c})$ is efficiently computable for any fixed w . We focus on demonstrating that this remains the case for CSA, specifically considering the case where individual view score functions take the form of the "GPCP"

Table 1: Average coverages across tasks for $\alpha = 0.10$ are shown in the top rows and average prediction set sizes in the bottom rows. Both were assessed over a batch of i.i.d. test samples (15% of the validation set from ImageNet). Standard deviations and means were computed across 10 randomized draws of the calibration and test sets.

Dataset	Models	ResNet	VGG	DenseNet	VFCP	\mathcal{C}^M	\mathcal{C}^R	\mathcal{C}^U	CSA
ImageNet	Coverage Size	0.901 (0.005) 137.004 (1.98)	0.902 (0.003) 136.116 (2.206)	0.902 (0.003) 120.096 (2.427)	0.899 (0.004) 46.063 (1.089)	0.938 (0.003) 87.337 (1.604)	0.909 (0.004) 82.746 (1.692)	0.9 (0.004) 131.856 (2.378)	0.9 (0.003) 34.006 (0.924)

score considered therein. In this setup, each constituent predictor is a generative model $q_k(C \mid X)$ from which $\{\hat{c}_{kj}\}_{j=1}^{J_k} \sim q_k(C \mid X)$ samples are drawn. Note that J_k need not be constant across k . The GPCP score, used to define the score components, is

$$s_k(x, c) = \min_{j \in 1, \dots, J_k} [d_k(\hat{c}_{kj}, c)], \quad (3)$$

where $d_k(\hat{c}, c)$ is a norm over the C space. Notably, this framework subsumes many standard regression settings, e.g., for a deterministic predictor, one can take $q_k(C \mid X) = \delta(f_k(X))$. To compute $\max_{\hat{c} \in \mathcal{C}(x)} f(w, \hat{c})$, we first let $\vec{j} \in \mathcal{J} = \{j_1, \dots, j_K\}$ be an indexing tuple, where each $j_k \in \{1, \dots, J_k\}$. That is, each \vec{j} is a vector that “selects” one sample per predictor. Notably then, the projection $u_m^\top s(\hat{c}_{\vec{j}}, c)$ is convex in c , since the projection directions are all restricted to \mathcal{S}_+^{K-1} . As a result, we can compute the maximizer c^* , since

$$\begin{aligned} c_{\vec{j}}^* &:= \arg \max_c f(w, c) \\ \text{s.t. } u_m^\top s(\hat{c}_{\vec{j}}, c) &\leq \hat{q}_m \quad \forall m \in \{1, \dots, M\} \end{aligned} \quad (4)$$

remains a standard convex optimization problem. The final maximum can then be found by aggregation, namely $c^* = \arg \max_{\vec{j} \in \mathcal{J}} f(w, c_{\vec{j}}^*)$. While $|\mathcal{J}| = \prod_{k=1}^K J_k$, we note that certain cases of ensemble prediction, such as multi-view prediction, tend to have a limited number of predictors in practice, most typically $K = 2$ or $K = 3$. This coupled with the fact that computing over these indices is trivially parallelizable means this approach is still computationally tractable. The full procedure is outlined in Algorithm 2.

Algorithm 2 Predict-Then-Optimize Under CSA

- 1: **Inputs:** Context x , Predictors $\{q_k(C \mid X)\}_{k=1}^K$, Optimization steps T , Sample counts $\{J_k\}_{k=1}^K$, CSA quantile $\{(u_m, \hat{q}_m)\}_{m=1}^M$
- 2: $\{\{\hat{c}_{kj}\}_{j=1}^{J_k} \sim q_k(C \mid X)\}_{k=1}^K, \mathcal{J} = \prod_{k=1}^K [J_k]$
- 3: $w^{(0)} \sim U(\mathcal{W})$
- 4: **for** $t \in \{1, \dots, T\}$ **do**
- 5: **for** $\vec{j} \in \mathcal{J}$ **do** $c_{\vec{j}}^* \leftarrow \arg \max_c f(w^{(t)}, c)$
 s.t. $\forall m \in 1, \dots, M \quad u_m^\top s(\hat{c}_{\vec{j}}, c) \leq \hat{q}_m$
- 6: $c^* \leftarrow \arg \max_{c_{\vec{j}}^*} f(w^{(t)}, c_{\vec{j}}^*)$
- 7: $w^{(t)} \leftarrow \Pi_{\mathcal{W}}(w^{(t-1)} - \eta \nabla_w f(w^{(t-1)}, c^*))$
- 8: **end for**
- 9: **Return** $w^{(T)}$

4 Experiments

We now study CSA empirically across several tasks, demonstrating its coverage guarantees with reduced conservatism. We demonstrate improvements in an ImageNet classification task in Section 4.1, in real-data UCI regression tasks as studied in [29] in Section 4.2, and in a downstream predict-then-optimize task in Section 4.3.

To allow for fair comparison, we note that the predictors and calibration and test sets were fixed across choices of calibration procedure for each experiment. This in turn means that some care had to be taken in partitioning $\mathcal{D}_C = \mathcal{D}_C^{(1)} \cup \mathcal{D}_C^{(2)}$ for CSA, where an insufficiently large $\mathcal{D}_C^{(1)}$ would result in poor estimation of the α -quantile envelope and hence require a large adjustment \hat{t} factor and an insufficiently large $\mathcal{D}_C^{(2)}$ in the classical reduced predictive efficiency from conformal prediction. For this reason, we fixed the split to be 20%-80% in experiments.

We herein compare against the methods presented in Section 2.4, namely the model selection of [27], the aggregation methods of [25], and the single weighted score projection (VFCP) of [40]. We specifically consider the following aggregation methods from [25]: the standard majority-vote \mathcal{C}^M , partially randomized thresholding \mathcal{C}^R , and fully randomized thresholding \mathcal{C}^U approaches, fully described in Appendix F. Notably, these methods do not lend themselves for use in the predict-then-optimize setting, so we eliminate them from consideration therein. Similarly, VFCP can only be applied in classification settings; we, thus, do not compare to it across the regression tasks. Code will be made public upon acceptance.

4.1 Classification Tasks

We first study the predictive efficiency of the aforementioned methods on the ImageNet classification task [44]. In particular, an ensemble was constructed from three separately trained deep learning architectures, namely ResNet-50, VGG-11, and DenseNet-121. Conformalization on the individual models was performed using the standard classification score function across all approaches, namely $s(x, y) = \sum_{j=1}^l \hat{f}(x)_{\pi_j(x)}$ where $y = \pi_l(x)$ and $\pi(x)$ is the permutation of $\{1, \dots, |\mathcal{Y}|\}$ that sorts $\hat{f}(x)$ from most to least likely. Calibration was performed using 85% of the ImageNet test set and assessment of the coverage and interval lengths on the remaining 15%, with 10 trials conducted over randomized draws of these calibration and test sets.

The results are presented in Table 1. We see that all the approaches exhibit the desired coverage guarantees. However, the CSA score approach consistently produce significantly smaller prediction regions than both the individually conformalized input views and alternate aggregation strategies.

4.2 UCI Regression Tasks

We now similarly study the predictive efficiency of CSA across a suite of regression tasks from the UCI repository [45] as studied by [29]. We specifically consider those tasks for which there are at least 1,000 samples; the complete list of tasks are provided in Appendix D. The data for each task were split with 80% for training, 10% for calibration, and 10% for testing coverage and interval lengths.

The problem setup was replicated from [29], in which four prediction methods were ensembled for each prediction task, namely an OLS model, a LASSO linear model, a random forest, and a multi-layer perceptron. A standard absolute value residual function was used as the score across all methods, namely $s(x, y) = |\hat{f}(x) - y|$. Prediction intervals could be explicitly constructed for the \mathcal{C}^M , \mathcal{C}^R , and \mathcal{C}^U aggregation methods. For assessing interval length for CSA, however, a discretized grid $\mathcal{G}_Y \subset \mathcal{Y}$ of coarseness Δy was considered, and an interval length estimate given by $\mathcal{L}(\mathcal{C}(x)) \approx \Delta y \cdot |\{y : y \in \mathcal{G}_Y, s(x, y) \in \hat{\mathcal{Q}}\}|$. 10 trials were conducted for each task, randomized over subset selections of the training, calibration, and test sets. We also present an ablation, labeled “CSA (Single-Stage),” to demonstrate the two-stage calibration described in Section 3.1 is necessary to retain coverage; this single-stage approach does not split \mathcal{S}_C and instead directly computes $\{\hat{q}_m\}$ on \mathcal{S}_C per Section 3.1.1.

A subset of the results are given in Table 2; the full set of results is deferred to Appendix D due to space limitations. As in the results presented in Section 4.1, we see that CSA retains the coverage guarantees typical of conformal prediction yet produces significantly smaller prediction intervals than both the individual models and the alternate aggregation strategies. We additionally see that the “CSA (Single-Stage)” approach fails to retain coverage, demonstrating the necessity of the two-stage calibration.

4.3 CSA Predict-Then-Optimize

We now study the use of CSA for a real-world predict-then-optimize traffic routing task, as studied in the conformal predict-then-optimize paper [36]. In this task, a time series of T previously observed precipitation readings are used to predict future precipitations and, in turn, anticipated traffic, as fully described in Appendix E. We consider the traffic routing problem for a fixed source-target pair (s, t) over the graph of Manhattan, where $|\mathcal{V}| = 4584$ and $|\mathcal{E}| = 9867$. Formally, such a problem seeks

$$\begin{aligned} w^*(x) &:= \min_w \max_{\hat{c} \in \mathcal{C}(x)} \hat{c}^T w \\ \text{s.t. } &w \in [0, 1]^{\mathcal{E}}, Aw = b, \mathcal{P}_{X,C}(C \in \mathcal{C}(X)) \geq 1 - \alpha \end{aligned} \tag{5}$$

where $x \in \mathbb{R}^{T \times H \times W}$ are the previous precipitation readings, $w_e \in \mathbb{R}^{|\mathcal{E}|}$ the traffic proportion routed along road e , $c \in \mathbb{R}^{|\mathcal{E}|}$ the transit times anticipated across roads, $A \in \mathbb{R}^{|\mathcal{V}| \times |\mathcal{E}|}$ the graph incidence matrix, and $b \in \mathbb{R}^{|\mathcal{V}|}$ the vector that specifies the routing problem, in which $b_s = 1$, $b_t = -1$, and $b_k = 0$ for s the travel source node, t the terminal node, and $k \notin \{s, t\}$ all other nodes.

Table 2: Average coverages across tasks for $\alpha = 0.05$ are shown in the top rows and average prediction set lengths in the bottom rows, both were assessed over a batch of i.i.d. test samples (10% of the datasets). Standard deviations and means were computed across 10 randomized draws of the training, calibration, and test sets. Note that, while the single-stage prediction regions are the smallest, they fail to achieve the desired coverage level and are, thus, precluded from comparison.

Dataset	Methods	Linear Model	LASSO	Random Forest	Neural Net	C^M	C^R	C^U	CSA (Single-Stage)	CSA
3droad	Coverage	0.947 (0.001)	0.947 (0.001)	0.948 (0.001)	0.95 (0.0)	0.945 (0.001)	0.915 (0.0)	0.948 (0.0)	0.926 (0.001)	0.95 (0.0)
3droad	Length	71.583 (0.325)	71.576 (0.331)	5.362 (0.006)	56.298 (0.602)	53.166 (0.482)	29.04 (0.245)	51.158 (0.015)	1.175 (0.036)	1.361 (0.031)
parkinsons	Coverage	0.948 (0.002)	0.951 (0.001)	0.935 (0.005)	0.942 (0.001)	0.946 (0.002)	0.878 (0.006)	0.937 (0.005)	0.857 (0.019)	0.961 (0.004)
parkinsons	Length	37.058 (0.599)	37.349 (0.34)	0.876 (0.11)	18.912 (0.931)	17.918 (0.814)	8.738 (0.427)	23.945 (0.039)	0.465 (0.196)	0.588 (0.188)
pol	Coverage	0.942 (0.007)	0.944 (0.007)	0.951 (0.002)	0.952 (0.001)	0.936 (0.006)	0.9 (0.009)	0.949 (0.003)	0.889 (0.007)	0.95 (0.003)
pol	Length	97.558 (0.808)	97.476 (1.0)	19.437 (0.374)	41.775 (1.306)	38.033 (1.092)	27.596 (0.77)	63.011 (0.894)	1.357 (0.019)	1.654 (0.032)
pumadyn32nm	Coverage	0.932 (0.008)	0.933 (0.008)	0.943 (0.004)	0.924 (0.011)	0.917 (0.008)	0.886 (0.013)	0.935 (0.008)	0.863 (0.018)	0.926 (0.006)
pumadyn32nm	Length	3.865 (0.043)	3.827 (0.061)	1.158 (0.005)	1.145 (0.012)	1.239 (0.011)	1.089 (0.013)	2.54 (0.029)	2.355 (0.124)	2.767 (0.076)
slice	Coverage	0.951 (0.001)	0.948 (0.001)	0.948 (0.0)	0.953 (0.003)	0.947 (0.0)	0.912 (0.0)	0.951 (0.002)	0.91 (0.004)	0.95 (0.001)
slice	Length	35.242 (0.099)	35.863 (0.057)	2.749 (0.059)	8.596 (0.412)	8.315 (0.382)	5.378 (0.216)	20.401 (0.162)	1.114 (0.025)	1.388 (0.02)

We then consider two probabilistic models for traffic prediction, namely one based on the classical probabilistic Lagrangian integro-difference approach (STEPS) of [46] and one on the modern latent diffusion model (LDM) approach of [47]. As a result of the higher inference cost of the latter, we consider the setup where $J_1 > J_2$, specifically with $J_1 = 4$ and $J_2 = 1$, which additionally serves to empirically highlight the flexibility of non-uniform sampling from predictors discussed in Section 3.2. As discussed in Section 4, the alternate aggregation strategies do not lend themselves for use in this setting. We, therefore, only compare CSA to the best model selection strategy, specifically by comparing to the separate conformalizations of the two constituent predictors. Each model was conformalized with Equation (3) taken to be the score, where d_k was set to be the standard 2-norm across both predictors, such that $s_1(x, c) = \min_{j \in 1, \dots, J_1} \|\hat{c}_{1j} - c\|_2$ for $q_1(C \mid x)$ and similarly for $q_2(C \mid x)$. We here evaluate the methods using the expected suboptimality gap proportion, $\Delta\% = \mathbb{E}_X[\Delta(X, C(X)) / \min_w f(w, C(X))]$, where Δ is defined as discussed in Section 2.3. This quantity measures the conservatism of the produced robust optimal value and is bounded in $[0, 1]$ in this setting.

Experiments were conducted with $|\mathcal{D}_C| = 200$. The suboptimality was then computed across 100 i.i.d. test samples. To, therefore, assess the improvement offered by CSA, we conduct two paired t-tests, with hypotheses

$$H_0 : \Delta\%_{\text{CSA}} = \Delta\%_{\text{STEPS}} \quad H_1 : \Delta\%_{\text{CSA}} < \Delta\%_{\text{STEPS}}$$

and similarly for $\Delta\%_{\text{LDM}}$ and $\Delta\%_{\text{CSA}}$. The coverages and results of such t-tests are provided in Table 3, from which we find that CSA significantly reduces the suboptimality after accounting for Bonferroni multiple testing. We see that, while conformalization of either of the two views individually already produces the desired coverage, CSA produces more informative prediction regions, and hence less conservative robust upper bounds.

Table 3: Coverages across tasks for $\alpha = 0.05$ are shown in the left table across both the individually conformalized and CSA fused approaches. P-values of the paired t-tests comparing gap proportions ($\Delta\%$) are shown in the right table. Both were computed over 100 i.i.d. test samples.

STEPS	LDM	CSA	H_1	p-value
0.981	0.962	0.968	$\Delta\%_{\text{CSA}} < \Delta\%_{\text{STEPS}}$	3.61×10^{-4}
			$\Delta\%_{\text{CSA}} < \Delta\%_{\text{LDM}}$	9.50×10^{-4}

5 Discussion

We have presented CSA, a framework for producing informative prediction regions in ensemble predictor pipelines. We additionally demonstrated the generality of the proposed pipeline in settings of both classification and robust predict-then-optimize regression tasks. This work suggests many directions for extension. One point of interest is the integration of CSA with other downstream regression applications. For instance, [48] proposed an end-to-end differentiable extension to [36]: extending CSA for integration to their framework would be of great interest. Additionally, given the prevalence of late-stage fusion in robotics applications, an exciting applied avenue of research would investigate the use of CSA in settings of robust control.

References

- [1] Robert E Schapire et al. A brief introduction to boosting. In *Ijcai*, volume 99, pages 1401–1406. Citeseer, 1999.
- [2] Cha Zhang and Yunqian Ma. *Ensemble machine learning*, volume 144. Springer, 2012.
- [3] Thomas G Dietterich. Ensemble methods in machine learning. In *International workshop on multiple classifier systems*, pages 1–15. Springer, 2000.
- [4] Lvmin Zhang, Anyi Rao, and Maneesh Agrawala. Adding conditional control to text-to-image diffusion models. In *Proceedings of the IEEE/CVF International Conference on Computer Vision*, pages 3836–3847, 2023.
- [5] Alec Radford, Jong Wook Kim, Chris Hallacy, Aditya Ramesh, Gabriel Goh, Sandhini Agarwal, Girish Sastry, Amanda Askell, Pamela Mishkin, Jack Clark, et al. Learning transferable visual models from natural language supervision. In *International conference on machine learning*, pages 8748–8763. PMLR, 2021.
- [6] Shiliang Sun. A survey of multi-view machine learning. *Neural computing and applications*, 23:2031–2038, 2013.
- [7] Jing Zhao, Xijiong Xie, Xin Xu, and Shiliang Sun. Multi-view learning overview: Recent progress and new challenges. *Information Fusion*, 38:43–54, 2017.
- [8] Xiaoqiang Yan, Shizhe Hu, Yiqiao Mao, Yangdong Ye, and Hui Yu. Deep multi-view learning methods: A review. *Neurocomputing*, 448:106–129, 2021.
- [9] Ye Yuan, Guangxu Xun, Kebin Jia, and Aidong Zhang. A multi-view deep learning framework for eeg seizure detection. *IEEE journal of biomedical and health informatics*, 23(1):83–94, 2018.
- [10] Yifeng Li, Fang-Xiang Wu, and Alioune Ngom. A review on machine learning principles for multi-view biological data integration. *Briefings in bioinformatics*, 19(2):325–340, 2018.
- [11] Ye Yuan, Guangxu Xun, Kebin Jia, and Aidong Zhang. A multi-view deep learning method for epileptic seizure detection using short-time fourier transform. In *Proceedings of the 8th ACM international conference on bioinformatics, computational biology, and health informatics*, pages 213–222, 2017.
- [12] Ramon F Brena, Antonio A Aguileta, Luis A Trejo, Erik Molino-Minero-Re, and Oscar Mayora. Choosing the best sensor fusion method: A machine-learning approach. *Sensors*, 20(8):2350, 2020.
- [13] Erik Blasch, Tien Pham, Chee-Yee Chong, Wolfgang Koch, Henry Leung, Dave Braines, and Tarek Abdelzaher. Machine learning/artificial intelligence for sensor data fusion—opportunities and challenges. *IEEE Aerospace and Electronic Systems Magazine*, 36(7):80–93, 2021.
- [14] Mary B Alatise and Gerhard P Hancke. A review on challenges of autonomous mobile robot and sensor fusion methods. *IEEE Access*, 8:39830–39846, 2020.
- [15] Mahesh Subedar, Ranganath Krishnan, Paulo Lopez Meyer, Omesh Tickoo, and Jonathan Huang. Uncertainty-aware audiovisual activity recognition using deep bayesian variational inference. In *Proceedings of the IEEE/CVF international conference on computer vision*, pages 6301–6310, 2019.
- [16] Junjiao Tian, Wesley Cheung, Nathaniel Glaser, Yen-Cheng Liu, and Zsolt Kira. Uno: Uncertainty-aware noisy-or multimodal fusion for unanticipated input degradation. In *2020 IEEE International Conference on Robotics and Automation (ICRA)*, pages 5716–5723. IEEE, 2020.
- [17] John Denker and Yann LeCun. Transforming neural-net output levels to probability distributions. *Advances in neural information processing systems*, 3, 1990.
- [18] Marton Havasi, Rodolphe Jenatton, Stanislav Fort, Jeremiah Zhe Liu, Jasper Snoek, Balaji Lakshminarayanan, Andrew M Dai, and Dustin Tran. Training independent subnetworks for robust prediction. *arXiv preprint arXiv:2010.06610*, 2020.
- [19] Andrey Malinin and Mark Gales. Predictive uncertainty estimation via prior networks. *Advances in neural information processing systems*, 31, 2018.
- [20] Rahul Rahaman et al. Uncertainty quantification and deep ensembles. *Advances in neural information processing systems*, 34:20063–20075, 2021.
- [21] Moloud Abdar, Farhad Pourpanah, Sadiq Hussain, Dana Rezazadegan, Li Liu, Mohammad Ghavamzadeh, Paul Fieguth, Xiaochun Cao, Abbas Khosravi, U Rajendra Acharya, et al. A review of uncertainty quantification in deep learning: Techniques, applications and challenges. *Information fusion*, 76:243–297, 2021.
- [22] Jesús Carrete, Adrián Montes-Campos, Ralf Wanzenböck, Esther Heid, and Georg KH Madsen. Deep ensembles vs committees for uncertainty estimation in neural-network force fields: Comparison and application to active learning. *The Journal of Chemical Physics*, 158(20), 2023.

[23] Anastasios N Angelopoulos and Stephen Bates. A gentle introduction to conformal prediction and distribution-free uncertainty quantification. *arXiv preprint arXiv:2107.07511*, 2021.

[24] Glenn Shafer and Vladimir Vovk. A tutorial on conformal prediction. *Journal of Machine Learning Research*, 9(3), 2008.

[25] Matteo Gasparin and Aaditya Ramdas. Conformal online model aggregation. *arXiv preprint arXiv:2403.15527*, 2024.

[26] Vladimir G Trunov and Vladimir V V'yugin. Online aggregation of conformal predictive systems. In *Conformal and Probabilistic Prediction with Applications*, pages 430–449. PMLR, 2023.

[27] Yachong Yang and Arun Kumar Kuchibhotla. Selection and aggregation of conformal prediction sets. *Journal of the American Statistical Association*, pages 1–13, 2024.

[28] VV V'yugin and VG Trunov. Online aggregation of conformal forecasting systems. *Journal of Communications Technology and Electronics*, 68(Suppl 2):S239–S253, 2023.

[29] Matteo Gasparin and Aaditya Ramdas. Merging uncertainty sets via majority vote. *arXiv preprint arXiv:2401.09379*, 2024.

[30] Peter J Rousseeuw and Anja Struyf. Computing location depth and regression depth in higher dimensions. *Statistics and Computing*, 8:193–203, 1998.

[31] Robert Serfling. Quantile functions for multivariate analysis: approaches and applications. *Statistica Neerlandica*, 56(2):214–232, 2002.

[32] Linglong Kong and Ivan Mizera. Quantile tomography: Using quantiles with multivariate data. *Statistica Sinica*, pages 1589–1610, 2012.

[33] Davy Paindaveine and Miroslav Šiman. On directional multiple-output quantile regression. *Journal of Multivariate Analysis*, 102(2):193–212, 2011.

[34] Marc Hallin, Davy Paindaveine, and Marianna Šiman. Multivariate quantiles and multiple-output regression quantiles: From ℓ_1 optimization to halfspace depth. *Annals of Statistics*, 38:635–669, 2010.

[35] Jesse C Cresswell, Yi Sui, Bhargava Kumar, and Noël Vouitsis. Conformal prediction sets improve human decision making. *arXiv preprint arXiv:2401.13744*, 2024.

[36] Yash Patel, Sahana Rayan, and Ambuj Tewari. Conformal contextual robust optimization. *arXiv preprint arXiv:2310.10003*, 2023.

[37] Shunichi Ohmori. A predictive prescription using minimum volume k-nearest neighbor enclosing ellipsoid and robust optimization. *Mathematics*, 9(2):119, 2021.

[38] Abhilash Reddy Chenreddy, Nymisha Bandi, and Erick Delage. Data-driven conditional robust optimization. *Advances in Neural Information Processing Systems*, 35:9525–9537, 2022.

[39] Chunlin Sun, Linyu Liu, and Xiaocheng Li. Predict-then-calibrate: A new perspective of robust contextual lp. *arXiv preprint arXiv:2305.15686*, 2023.

[40] Rui Luo and Zhixin Zhou. Weighted aggregation of conformity scores for classification. *arXiv preprint arXiv:2407.10230*, 2024.

[41] Stefan Schnabel and Wolfhard Janke. A simple algorithm for uniform sampling on the surface of a hypersphere. *arXiv preprint arXiv:2204.14004*, 2022.

[42] Renukanandan Tumu, Matthew Cleaveland, Rahul Mangharam, George J Pappas, and Lars Lindemann. Multi-modal conformal prediction regions by optimizing convex shape templates. *arXiv preprint arXiv:2312.07434*, 2023.

[43] Shai Feldman, Stephen Bates, and Yaniv Romano. Calibrated multiple-output quantile regression with representation learning. *Journal of Machine Learning Research*, 24(24):1–48, 2023.

[44] Jia Deng, Wei Dong, Richard Socher, Li-Jia Li, Kai Li, and Li Fei-Fei. Imagenet: A large-scale hierarchical image database. In *2009 IEEE conference on computer vision and pattern recognition*, pages 248–255. Ieee, 2009.

[45] Arthur Asuncion, David Newman, et al. Uci machine learning repository, 2007.

[46] Seppo Pulkkinen, Daniele Nerini, Andrés A Pérez Hortal, Carlos Velasco-Forero, Alan Seed, Urs Germann, and Loris Foresti. Pysteps: An open-source python library for probabilistic precipitation nowcasting (v1. 0). *Geoscientific Model Development*, 12(10):4185–4219, 2019.

- [47] Zhihan Gao, Xingjian Shi, Boran Han, Hao Wang, Xiaoyong Jin, Danielle Maddix, Yi Zhu, Mu Li, and Yuyang Bernie Wang. Prediff: Precipitation nowcasting with latent diffusion models. *Advances in Neural Information Processing Systems*, 36, 2024.
- [48] Abhilash Chenreddy and Erick Delage. End-to-end conditional robust optimization. *arXiv preprint arXiv:2403.04670*, 2024.
- [49] Geoff Boeing. Modeling and analyzing urban networks and amenities with osmnx. 2024.

A CSA Visual Walkthrough

We walk through a visual presentation of the approach below to supplement the textual description in the main text. We start with a collection of multivariate calibration scores \mathcal{S}_C with $s \in \mathcal{S}$ being $\in \mathbb{R}^K$. For the purposes of visualization in this section, we have $K = 2$. We first partition the score evaluations $\mathcal{S}_C = \mathcal{S}_C^{(1)} \cup \mathcal{S}_C^{(2)}$, with a subset $\mathcal{S}_C^{(1)}$ used to define the pre-ordering and the remainder $\mathcal{S}_C^{(2)}$ to define the multivariate quantile.

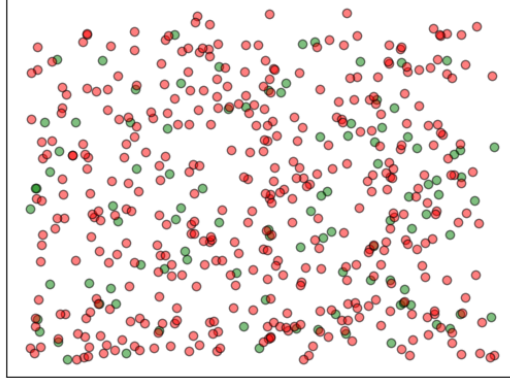


Figure 2: The calibration score evaluations are first split between those used to define the pre-ordering (green) $\mathcal{S}_C^{(1)}$ and those used to define the final multivariate quantile (red) $\mathcal{S}_C^{(2)}$.

We first wish to define the pre-ordering over $\mathcal{S}_C^{(1)}$. As described in the main text, the goal is to define this using an indexed family of sets \mathcal{A}_t with index $t \in \mathbb{R}$, after which the multivariate quantile approach reduces to the univariate quantile formulation. To ensure the final envelope over $\mathcal{S}_C^{(2)}$ remains as tight as possible, we wish to define this family in a data-driven fashion. Critically, the *shape* of this tightest envelope around $\mathcal{S}_C^{(2)}$ will vary across α , meaning we must define the family *separately* for each choice of α . We expect the contour of the tightest α envelope for $\mathcal{S}_C^{(1)}$ will be similar to that over $\mathcal{S}_C^{(2)}$, motivating such a choice to define the indexing family. To do this, we project $\mathcal{S}_C^{(1)}$ along a number of directions, finding the β quantile along each, in turn defining a half-plane, where β is as described in Section 3.1.

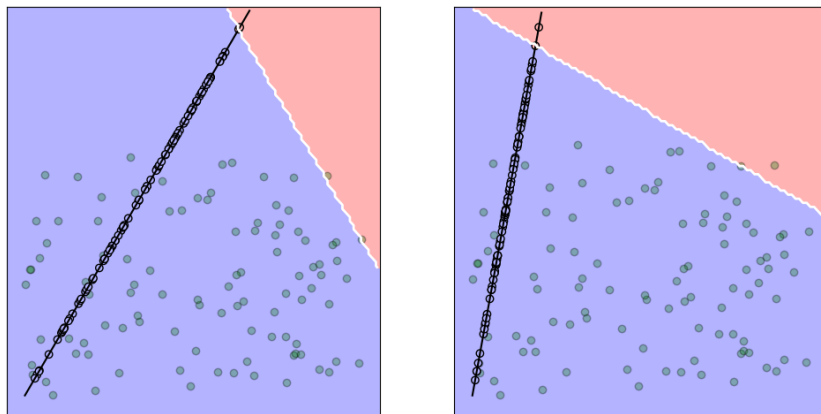


Figure 3: The pre-ordering points are projected across a number of directions, after which the β quantile is used to define a direction quantile. This defines a half-plane of points that are in the region (blue) and those outside (red).

We then iteratively update β in the manner described in Algorithm 1 to obtain β^* , namely the minimum value for which the region given by the intersection of the corresponding half-planes covers roughly $1 - \alpha$ of $\mathcal{S}_C^{(1)}$.

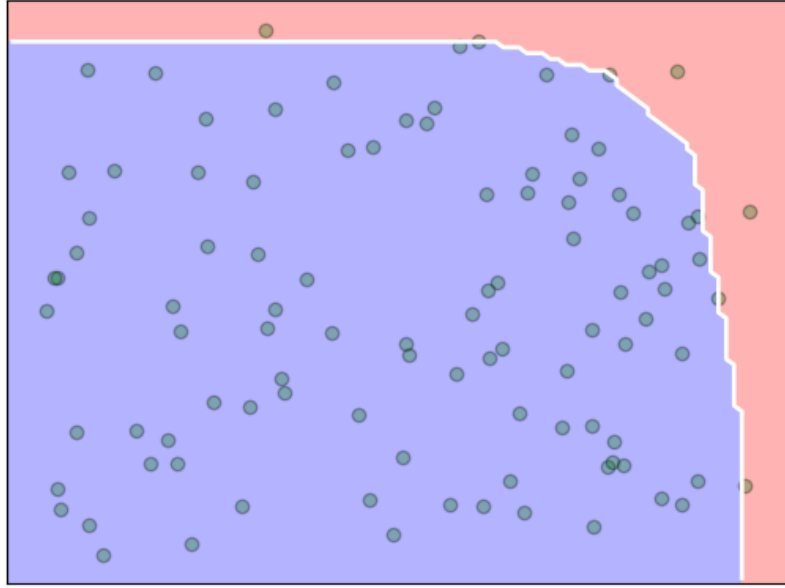


Figure 4: We use the intersection of hyperplanes to define the quantile envelope, seeking β^* that achieves the desired coverage.

Once this $1 - \alpha$ quantile envelope of $\mathcal{S}_C^{(1)}$ is found, we define \mathcal{A}_1 to be such an envelope, with which future points can now be partially ordered. That is, for any point $s \in \mathbb{R}^K$ notice that we can unambiguously associate it with $t(s) := \min\{t \in \mathbb{R} : s \in \mathcal{A}_t\}$. Intuitively, this is the t where the contour ‘‘intersects’’ s . Notably, now that the partial ordering has been defined, the points of $\mathcal{S}_C^{(1)}$ are no longer used. It would be of interest to investigate whether a concurrent definition of the partial ordering and final calibration is possible without such data splitting in future work.

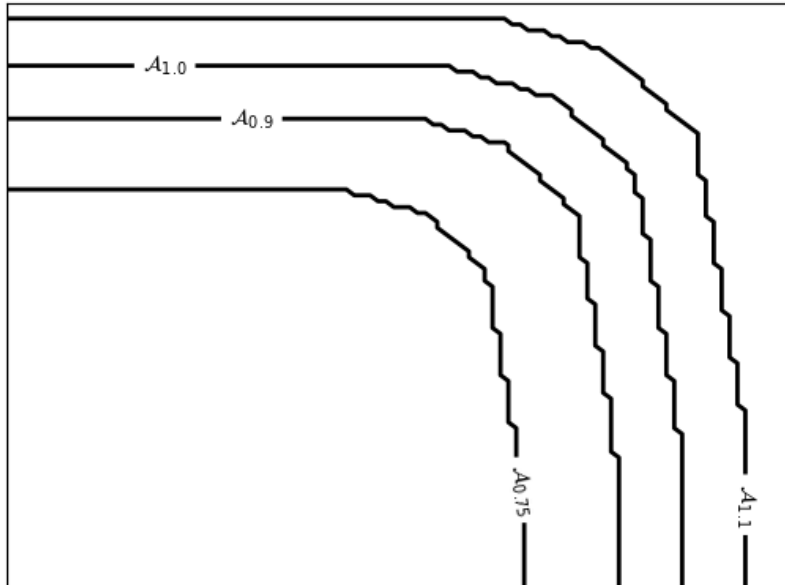


Figure 5: Using the quantile envelope, the family of nested sets \mathcal{A}_t is defined, in turn defining a partial ordering over \mathbb{R}^K .

With this \mathcal{A}_t , we find the final \hat{q} simply by mapping the points of $\mathcal{S}_C^{(2)}$ to their corresponding $t(s)$ values in the aforementioned fashion and performing standard conformal prediction. As discussed, if the envelope has a similar structure to that found over $\mathcal{S}_C^{(1)}$, the envelope should be adjusted by only a minor amount.

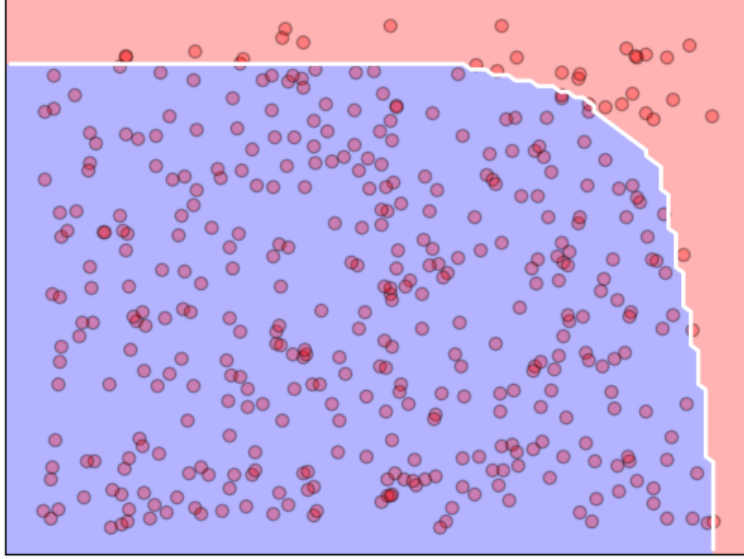


Figure 6: Using the nested family of sets, we expand or contract the envelope appropriately using the data of $\mathcal{S}_C^{(2)}$ to find the final adjustment factor.

B Multivariate Score Coverage

The proof of the multivariate extension of conformal prediction follows in precisely the same manner as that of standard conformal prediction with the pre-order \lesssim replacing the complete ordering used in traditional conformal prediction.

Theorem B.1. Suppose $\mathcal{D}_C := \{(X_i, Y_i)\}_{i=1}^{N_C}$ and (X', Y') are exchangeable. Assume further that K maps $s_k : \mathcal{X} \times \mathcal{Y} \rightarrow \mathbb{R}$ have been defined and a composite $s(X, Y) := (s_1(X, Y), \dots, s_K(X, Y))$ is defined. Further denote by \mathcal{S}_C the evaluation of $s(X, Y)$ on \mathcal{D}_C , namely $\mathcal{S}_C := \{s(X_i, Y_i) \mid (X_i, Y_i) \in \mathcal{D}_C\}$. For some $\alpha \in (0, 1)$, given a pre-order \lesssim in \mathbb{R}^K induced by a collection of nested sets $\{\mathcal{A}_t\}_{t \geq 0}$ define $\mathcal{Q}(\alpha) = \{s \in \mathbb{R}^K : s \lesssim s_{\lceil (N_C+1)(1-\alpha) \rceil}\}$. Then, denoting $\mathcal{C}(x) := \{y : s(x, y) \in \mathcal{Q}(\alpha)\}$,

$$\mathcal{P}_{X', Y'}(Y' \in \mathcal{C}(X')) \geq 1 - \alpha \quad (6)$$

Proof. Denote $s_i = s(X_i, Y_i)$ for each $i = 1, \dots, n$ and $s' = s(X', Y')$. We define $t_i = \inf\{t \geq 0 : s_i \in \mathcal{A}_t\}$ and $t' = \inf\{t \geq 0 : s' \in \mathcal{A}_t\}$. We consider the case that $\mathcal{P}_{X, Y}(t_i \neq t_j) = 1$, that is, that the probability of ties is a probability measure 0 set. Without loss of generality, we then assume the scores are sorted according to the assumed pre-order, namely that $s_1 \lesssim s_2 \lesssim \dots \lesssim s_{N_C}$, or equivalently $t_1 \leq t_2 \leq \dots \leq t_{N_C}$. We then again have that $\hat{t} = t_{\lceil (N_C+1)(1-\alpha) \rceil}$ if $\alpha > 1/(N_C + 1)$ and $\hat{t} = \infty$ otherwise. In the latter case, coverage is trivially satisfied. In the former case, we see

$$\mathcal{P}_{X, Y}(Y' \in \mathcal{C}(X')) = \mathcal{P}_{X, Y}(s(X, y) \lesssim s_{\lceil (N_C+1)(1-\alpha) \rceil}) = \mathcal{P}_{X, Y}(t' \leq t_{\lceil (N_C+1)(1-\alpha) \rceil}). \quad (7)$$

By the assumed exchangeability of $\mathcal{D}_C := \{(X_i, Y_i)\}_{i=1}^{N_C}$ and (X', Y') , we have that

$$\mathcal{P}_{X, Y}(t' \leq t_k) = \frac{k}{N_C + 1}, \quad (8)$$

for any k . From here, we have the desired conclusion that

$$\mathcal{P}_{X, Y}(s(X, y) \lesssim s_{\lceil (N_C+1)(1-\alpha) \rceil}) = \left(\frac{1}{N_C + 1} \right) (\lceil (N_C + 1)(1 - \alpha) \rceil) \geq 1 - \alpha, \quad (9)$$

completing the proof as desired. \square

C CSA Predict-Then-Optimize Visual Walkthrough

We now present a visual accompaniment of the predict-then-optimize algorithm presented in Section 3.2. We once again take $K = 2$ for visual clarity in this walkthrough, where the predictors are as discussed in Section 3.2, namely assumed to be generative predictors $q_k(C \mid X)$ where the number of samples per predictor are fixed to be $\{J_k\}$. For illustration, we assume $J_1 = 5$ and $J_2 = 3$, meaning predictions with the first model are made by drawing 5 samples and 3 for the second. We assume the CSA calibration of Section 3.1 has already been performed, from which a collection of projection directions and quantiles $\{(u_m, \hat{q}_m)\}_{m=1}^M$ are available that implicitly define an acceptance region $\hat{\mathcal{Q}}$. We further assume the individual predictor score functions are all the GPCP score given in Equation (3), with d_k from Equation (3) specifically here taken to simply be the standard Euclidean 2-norm, giving

$$s_k(x, c) = \min_{j \in 1, \dots, J_k} \|\hat{c}_{kj} - c\|. \quad (10)$$

We now wish to compute $c^* = \max_{\hat{c} \in \mathcal{C}(x)} f(w, \hat{c})$. To do so, we must start by defining this region $\mathcal{C}(x)$ for the test point x , which we do by drawing the respective number of samples from the two models, producing samples $\{\hat{c}_{1j}\}_{j=1}^5$ and $\{\hat{c}_{2j}\}_{j=1}^3$, as shown in Figure 7.

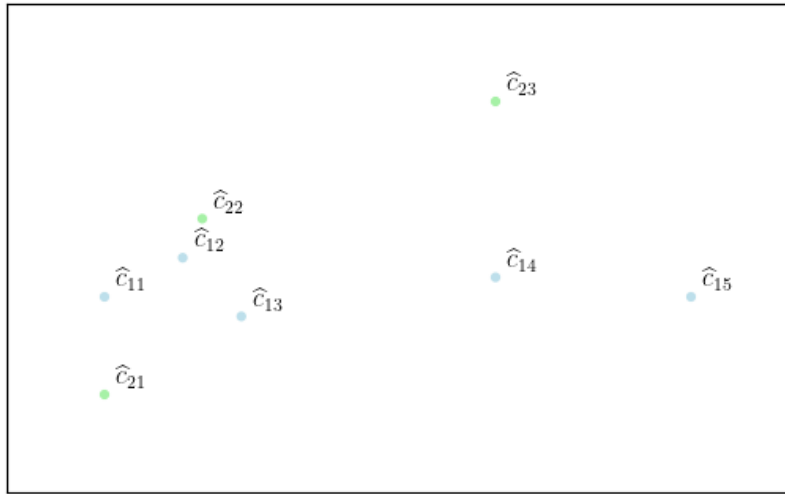


Figure 7: Samples drawn from the two generative models $\{\hat{c}_{1j}\}_{j=1}^5 \sim q_1(C \mid x)$ (blue) and $\{\hat{c}_{2j}\}_{j=1}^3 \sim q_2(C \mid x)$ (green). Note that this is a visualization in the \mathcal{C} space, i.e. *not* the space of multivariate scores.

By definition, $\forall c \in \mathcal{C}(x)$,

$$u_m^\top \left(\min_{j_1=1, \dots, 5} \|\hat{c}_{1j_1} - c\|, \min_{j_2=1, \dots, 3} \|\hat{c}_{2j_2} - c\| \right) \leq \hat{q}_m \quad \forall m = 1, \dots, M. \quad (11)$$

As a result, we must have that, $\forall c \in \mathcal{C}(x)$, $\exists j_1 = 1, \dots, 5$ and $j_2 = 1, \dots, 3$ such that $u_m^\top (\|\hat{c}_{1j_1} - c\|, \|\hat{c}_{2j_2} - c\|) \leq \hat{q}_m \quad \forall m = 1, \dots, M$. Solving for c^* , therefore, amounts to considering each pair $\vec{j} := (j_1, j_2) \in \mathcal{J}$, where $\mathcal{J} := \{1, \dots, 5\} \times \{1, \dots, 3\}$, and solving

$$\begin{aligned} c_{\vec{j}}^* &:= \arg \max_c f(w, c) \\ \text{s.t.} \quad u_m^\top \left(\|\hat{c}_{1j_1} - c\|, \|\hat{c}_{2j_2} - c\| \right) &\leq \hat{q}_m \quad \forall m \in \{1, \dots, M\} \end{aligned} \quad (12)$$

Notice that, for any fixed \vec{j} , this is a standard convex optimization problem with a convex feasible region. We illustrate how the feasible region would be constructed for a fixed \vec{j} in Figure 8. Note that the construction of this feasible is never explicitly done in practice and is only implicitly used by convex solver routines in practice.

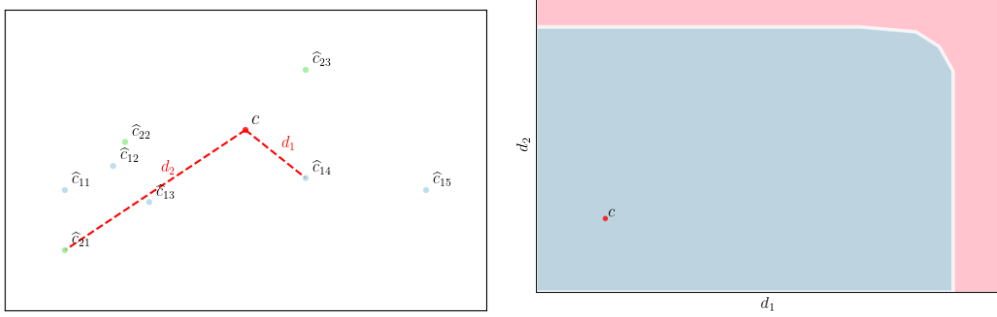


Figure 8: A candidate $c \in \mathcal{C}$ is in prediction region if the projections of its distances (d_1, d_2) from *at least one* pair of points indexed by $\vec{j} := (j_1, j_2)$ is in the acceptance region $\widehat{\mathcal{Q}}$. Here, we illustrate a point c that lies in the feasible region from its proximity to the $\vec{j} := (4, 1)$ pair of points. Note that the left is again a visualization over the \mathcal{C} space, whereas the right is of the *score* space.

We can, therefore, then solve Equation (12) over all possible $\vec{j} \in \mathcal{J}$ and aggregate the maxima to compute c^* .

D Additional UCI Results

We consider those regression tasks from the UCI repository [45] that have at least 1,000 samples. The complete list of tasks considered herein is provided in Table 4.

Table 4: Tasks considered for empirical validation of prediction region efficiency and coverage, along with their relevant dimensions. All tasks are scalar regression tasks, i.e. $y \in \mathbb{R}$.

Dataset	Observations	Input Dimension
3droad	434874	3
airfoil	1503	5
bike	17379	17
parkinsons	5875	20
pol	15000	26
pumadyn32nm	8192	32
slice	53500	385

The complete collection of results is presented in Table 5. As in the main text, we see reduced conservatism of the CSA prediction regions compared to alternatives. We additionally notice that the single-stage CSA approach fails to retain the coverage guarantees.

Table 5: Average coverages across tasks for $\alpha = 0.05$ are shown in the top row and average prediction set lengths in the bottom row, where both were assessed over a batch of i.i.d. test samples (10% of the dataset size). Standard deviations and means were computed across 10 randomizations of draws of the training, calibration, and test sets. Note that, while the single-stage prediction regions are the smallest, they fail to achieve the desired coverage level and are, therefore, precluded from comparison.

Dataset	Methods	Linear Model	LASSO	Random Forest	Neural Net	\mathcal{C}^M	\mathcal{C}^R	\mathcal{C}^U	CSA (Single-Stage)	CSA
3droad	Coverage	0.947 (0.001)	0.947 (0.001)	0.948 (0.001)	0.95 (0.0)	0.945 (0.001)	0.915 (0.0)	0.948 (0.0)	0.926 (0.001)	0.95 (0.0)
	Length	71.583 (0.325)	71.576 (0.331)	5.362 (0.006)	56.298 (0.602)	53.166 (0.482)	29.04 (0.245)	51.158 (0.015)	1.175 (0.036)	1.361 (0.031)
airfoil	Coverage	0.95 (0.012)	0.981 (0.018)	0.954 (0.02)	0.969 (0.014)	0.962 (0.014)	0.939 (0.024)	0.969 (0.014)	0.854 (0.04)	0.952 (0.006)
	Length	18.742 (0.313)	25.218 (1.05)	7.353 (0.672)	25.256 (1.424)	18.097 (0.565)	11.96 (0.634)	18.303 (0.787)	1.873 (0.21)	2.714 (0.141)
bike	Coverage	0.963 (0.004)	0.959 (0.004)	0.948 (0.001)	0.955 (0.003)	0.955 (0.003)	0.932 (0.008)	0.959 (0.003)	0.946 (0.005)	0.955 (0.003)
	Length	3.397 (0.131)	3.416 (0.123)	0.025 (0.0)	1.716 (0.104)	1.654 (0.11)	0.837 (0.055)	2.094 (0.09)	0.569 (0.097)	0.629 (0.105)
parkinsons	Coverage	0.948 (0.002)	0.951 (0.001)	0.935 (0.005)	0.942 (0.001)	0.946 (0.002)	0.878 (0.006)	0.937 (0.005)	0.857 (0.019)	0.961 (0.004)
	Length	37.058 (0.599)	37.349 (0.34)	0.876 (0.11)	18.912 (0.931)	17.918 (0.814)	8.738 (0.427)	23.945 (0.039)	0.465 (0.196)	0.588 (0.188)
pol	Coverage	0.942 (0.007)	0.944 (0.007)	0.951 (0.002)	0.952 (0.001)	0.936 (0.006)	0.9 (0.009)	0.949 (0.003)	0.889 (0.007)	0.95 (0.003)
	Length	97.558 (0.808)	97.476 (1.0)	19.437 (0.374)	41.775 (1.306)	38.033 (1.092)	27.596 (0.77)	63.011 (0.894)	1.357 (0.019)	1.654 (0.032)
pumadyn32nm	Coverage	0.932 (0.008)	0.933 (0.008)	0.943 (0.004)	0.924 (0.011)	0.917 (0.008)	0.886 (0.013)	0.935 (0.008)	0.863 (0.018)	0.926 (0.006)
	Length	3.865 (0.043)	3.827 (0.061)	1.158 (0.005)	1.145 (0.012)	1.239 (0.011)	1.089 (0.013)	2.54 (0.029)	2.355 (0.124)	2.767 (0.076)
slice	Coverage	0.951 (0.001)	0.948 (0.001)	0.948 (0.0)	0.953 (0.003)	0.947 (0.0)	0.912 (0.0)	0.951 (0.002)	0.91 (0.004)	0.95 (0.001)
	Length	35.242 (0.099)	35.863 (0.057)	2.749 (0.059)	8.596 (0.412)	8.315 (0.382)	5.378 (0.216)	20.401 (0.162)	1.114 (0.025)	1.388 (0.02)

E Robust Traffic Routing Setup

We replicate the experimental setup of [36], namely where a graph of Manhattan with corresponding nominal transit times was extracted using OSMnx [49]. Formally, the Manhattan graph is given as a tuple $(\mathcal{V}, \mathcal{E})$, where the edge weights represent the transit times along the respective city roads. Such weights were assigned in a two-step process, namely by first making weather predictions and then using such weather predictions to then upweight the nominal transit times. In particular, precipitation forecasts were made from time-series observations of previous precipitations readings, specifically given over a map spatially resolved to $H \times W$ resolution. Precipitation forecasters, such as those considered in the experiments herein as given in [46] and [47], specifically map such previous observations to potential future trajectories. Formally, they define probabilistic models over some future time horizon T_f , from which probabilistic draws $\tilde{Y} \in \mathbb{R}^{T_f \times H \times W} \sim \mathcal{P}(\tilde{Y} | x)$ can be made, where $x \in \mathbb{R}^{T \times H \times W}$. Notably, we instead consider the probabilistic forecasts at some future *fixed* time point T' , meaning the outcome of interest $Y \in \mathbb{R}^{H \times W} = \tilde{Y}_{T'}$.

From a precipitation map, namely a spatially resolved reading $Y \in \mathbb{R}^{H \times W}$, we assign the final edge weights by first associating nodes to the closest pixel coordinate of the precipitation map. That is, denoting the pixel nearest to a vertex v as (p_x^v, p_y^v) , the node is assigned the value at such a spatial location $Y_{p_x^v, p_y^v}$. To, therefore, assign the edge weight, we average the weights of the edge endpoints and then weigh the nominal transit time. In particular, denoting the nominal transit time along such an edge e between nodes (s, t) as \tilde{c}_e , the transit time with traffic was computed as

$$c_e := \tilde{c}_e \cdot \exp \left\{ \frac{Y_{p_x^s, p_y^s} + Y_{p_x^t, p_y^t}}{2} \right\}. \quad (13)$$

F Conformal Aggregation Methods

We now describe the methods from [25] that were compared against experimentally, specifically the standard majority-vote \mathcal{C}^M , partially randomized thresholding \mathcal{C}^R , and fully randomized thresholding \mathcal{C}^U approaches. As discussed in Section 2.4, these methods all follow the structural form of Equation (2) and largely differ in their choice of weights and thresholds. The standard majority-vote \mathcal{C}^M is the most natural choice, defined by

$$\mathcal{C}^M(x) := \left\{ y \mid \frac{1}{K} \sum_{k=1}^K \mathbb{1}[y \in \mathcal{C}_k(x)] > \frac{1}{2} \right\}. \quad (14)$$

The randomized methods differ in that independent randomization is leveraged over the threshold, namely with:

$$\mathcal{C}^R(x) := \left\{ y \mid \frac{1}{K} \sum_{k=1}^K \mathbb{1}[y \in \mathcal{C}_k(x)] > \frac{1}{2} + \frac{U}{2} \right\} \quad (15)$$

$$\mathcal{C}^U(x) := \left\{ y \mid \frac{1}{K} \sum_{k=1}^K \mathbb{1}[y \in \mathcal{C}_k(x)] > U \right\}, \quad (16)$$

for $U \sim \text{Unif}([0, 1])$. Notably, all these methods retain the guarantees typical of conformal prediction.